The University of Southern Mississippi
The Aquila Digital Community

Faculty Publications

2-22-2005

A Study of Wave Effects On Wind Stress Over the Ocean In a Fetch-Limited Case

Jiayi Pan
University of Southern Mississippi

David W. Wang
Stennis Space Center

Paul A. Hwang
Stennis Space Center

Follow this and additional works at: http://aquila.usm.edu/fac_pubs

Part of the Marine Biology Commons

Recommended Citation

A study of wave effects on wind stress over the ocean in a fetch-limited case

Jiayi Pan[1]

Department of Marine Science, University of Southern Mississippi, Stennis Space Center, Mississippi, USA

David W. Wang and Paul A. Hwang

Oceanography Division, Naval Research Laboratory, Stennis Space Center, Mississippi, USA

[1]   A field experiment was conducted for collecting three-dimensional wind, wave, and air-sea environmental data off the coast of Louisiana in the Gulf of Mexico in the mixed sea state of a wind sea limited by fetch and with swell propagating against the wind direction. Two methods, the inertial dissipation (ID) and eddy correlation (EC), are used to calculate wind stress. The results show that under the fetch-limited condition, the EC wind stress is greater than the ID stress. This difference is found to be correlated with the counter-wind swell. The swell-related drag coefficient is computed from the wind stress difference between the ID and EC methods. An empirical formula is constructed for the swell-related drag coefficient with a regression coefficient of 0.71. The swell-related drag coefficient is proportional to the swell steepness ($k_p H_s$) and inversely proportional to the ratio of the wind speed and the swell peak phase speed (U_{10}/C_p).

Citation: Pan, J., D. W. Wang, and P. A. Hwang (2005), A study of wave effects on wind stress over the ocean in a fetch-limited case, *J. Geophys. Res.*, *110*, C02020, doi:10.1029/2003JC002258.

1.   Introduction

[2]   Wind stress plays an important role in the momentum exchange between the atmosphere and ocean. Accurate knowledge of the wind stress is of increasing importance in ocean and atmospheric modeling and dynamic studies. Conventionally, wind stress is parameterized by the bulk formula

$$\tau = \rho \, C_z U_z^2, \tag{1}$$

where τ is the wind stress; ρ is the air density; C_z is drag coefficient, and U_z is the horizontal wind speed at the height z above the ocean surface. In this study, C_z and U_z represent the drag coefficient and wind speed in neutral stability condition, respectively. The vertical profile of wind speed with height is given by [*Csanady*, 2001]

$$U_z = \frac{u_*}{\kappa} \ln\left(\frac{z}{z_0}\right), \tag{2}$$

where u_* is the friction wind speed defined by $(\tau/\rho)^{1/2}$, κ is the von Kármán constant, and z_0 is aerodynamic roughness length (hereinafter referred to as roughness).

The drag coefficient C_z can be expressed by the roughness z_0,

$$C_z = \frac{\kappa^2}{\ln^2 (z/z_0)}. \tag{3}$$

Equation (3) shows a unique and monotonous relationship between C_z and z_0, which suggests equivalence between C_z and z_0 in describing the parameterization of the wind stress over the ocean. When roughness increases (decreases), the drag coefficient also increases (decreases).

[3]   The wind stress parameterization coefficient (drag coefficient) has been explored extensively since the parameterization form of equation (1) was introduced. Early investigators suggested that the drag coefficient could be a constant [*Paulson et al.*, 1972; *Hidy*, 1972]. Later studies showed that C_z is wind speed dependent [*Garratt*, 1977; *Smith*, 1980]. *Large and Pond* [1981] suggested that C_{10} (the neutral drag coefficient at 10 m height) is a constant in U_{10} between 4 and 11 m/s, and increases linearly with U_{10} between 11 and 25 m/s. *Charnock* [1955] proposed an expression for the roughness

$$z_0 = a \frac{u_*^2}{g}, \tag{4}$$

where g is the acceleration of gravity, and a is known as the Charnock constant between 0.012 and 0.035 [*Wu*, 1980]. The Charnock constant seemed to be dependent on wind speed, viscosity, and surface tension [*Wu*, 1980]. *Stewart*

---

[1]Now at Department of Environmental and Biomolecular Systems, Oregon Graduate Institute, Beaverton, Oregon, USA.

[1974] found that the Charnock constant is related to the wave age, and suggested that the Charnock relation should be modified to

$$z_0 = \frac{u_*^2}{g} f\left(\frac{c_p}{u_*}\right),$$ (5)

where c_p is the peak phase speed of the ocean wave, and c_p/u_* represents the wave age. The wave parameter, wave age, in equation (5) indicates effects of ocean waves on wind stress.

[4] *Donelan* [1990] introduced a dimensionless roughness by scaling z_0 with the root-mean square (rms) wave height σ, and concluded that the dimensionless roughness is inversely proportional to wave age on the basis of field data, which means that younger waves (traveling slower than the wind) are rougher than mature waves. This conclusion was also supported by the wind stress data of Humidity Exchange over the Sea (HEXOS) collected in the North Sea [*Smith et al.*, 1992]. Employing wind stress data in Lake Ontario and HEXOS, *Donelan et al.* [1993] obtained a regression formula for the pure wind sea,

$$\frac{z_0}{\sigma} = A\left(\frac{U_{10}}{c_p}\right)^B,$$ (6)

with regression coefficients $A = 6.7 \times 10^{-4}$ and $B = 2.6$. Using several combined field wind stress data, *Drennan et al.* [1999a, 2003] gave a similar relationship between dimensionless roughness and wave age, but with different regression coefficients. *Janssen* [1989] proposed a semi-theoretical and semi-empirical explanation for the wave age dependence of the roughness for the developing wind sea. In the open ocean, it was reported that no clear dependence of the roughness on wave age exists [*Dobson et al.*, 1994; *Yelland and Taylor*, 1996], though *Dobson et al.* [1994] used a technique to filter out the swell and leave the wind sea for analysis. In addition to the wave age dependence, the wind stress was found to be dependent on wave steepness [*Anctil and Donelan*, 1996; *Taylor and Yelland*, 2001]. Using a single formula,

$$\frac{z_0}{H_s} = A\left(\frac{H_s}{L_p}\right)^B,$$ (7)

Taylor and Yelland [2001] could simulate both field and laboratory wind stress data. In equation (7), H_s is the significant wave height and L_p is the spectrum peak wavelength. However, it was found that field and laboratory wind stress data have different dependence of roughness on wave age [*Donelan et al.*, 1993].

[5] Recent studies also showed swell influences on wind stress and roughness. *Dobson et al.* [1994] observed the cases of swell running against the wind. *Donelan et al.* [1997] reported direct observations of wind stress and wave directional properties during the Surface Wave Dynamic Experiment (SWADE). Their results indicated that the drag coefficient in the presence of counter and cross swells can be different from that for a pure wind sea. *Drennan et al.* [1999a] examined the wind stress measured on 3-m discus buoys in the SWADE and High-Resolution Remote Sensing

(High-Res) Experiments, and found that much of the scatter in the drag coefficient is attributed to swell effects. *Hwang* [2004] demonstrated that the parameterization of drag coefficient and surface roughness can be significantly improved by using wavelength instead of 10 m as the reference length scale of atmospheric measurements.

[6] Although several studies showed that the wind stress over the ocean is affected by sea surface waves, the quantitative relationships between the wind stress and wave parameters are still unsettled. More field experiments are needed to reveal details of wave effects on the wind stress, especially to quantify the swell effects on the drag coefficient. *Drennan et al.* [1999b] found that in the presence of swell, the wind stress within the wave boundary layer (WBL) is different from that outside the WBL. Their study revealed that wave effects are strong within the WBL, which is about 1 m height. *Donelan and Dobson* [2001] demonstrated that the wave-coherent wind stress is more pronounced near the surface. However, most field observations were taken higher than 5 m above the ocean surface. It is believed that wind stress measurements closer to the ocean surface can better address the wave-induced wind stress.

[7] In this study, we report a field experiment collecting wind stress data at 1.5 m height above the sea surface with a sonic anemometer mounted on a free-drifting, wave-following platform. The wave parameters were simultaneously measured by thin wire gauges. Section 2 describes the field experiment and data. The two wind stress calculation methods, inertial dissipation and eddy correlation, are outlined in section 3. Section 4 gives results and analyses. Sections 5 to 7 present discussions on error analysis, flow distortion, and swell influence on the wind stress. A summary is given in section 8.

2. Instruments and Field Experiment

2.1. Instruments

[8] The data used in this study were collected by sensors mounted on a free-drifting buoy following the design by *Hwang et al.* [1996]. The instruments include a three-dimensional (3-D) ultrasonic anemometer, wave gauge arrays (WGA), environmental sensors (ES), and system dynamics sensors (SD). The ultrasonic anemometer (R M Young 81000) is mounted in the buoy frame for providing measurements of wind velocity vectors in three directions. The wave gauge arrays are made from two sets of 20 capacitance wave-height sensors using the design by *Chapman and Monaldo* [1995]. The resolution of the water height measurement is 0.25 mm. The Environmental Sensor system records the following parameters: water temperature, air temperature and humidity, and buoy position. The System Dynamics sensors measure the buoy motion. The following parameters are recorded: two-horizontal tilt components, three-dimensional acceleration components, and the compass reading. More discussions on the instrumentation have been given by *Hwang and Wang* [2004] and *Wang and Hwang* [2004].

2.2. Field Experiment

[9] The experiment was conducted off the coast of Louisiana in the Gulf of Mexico. After a cold front moved into the area on 16 February 2003, the wind shifted to
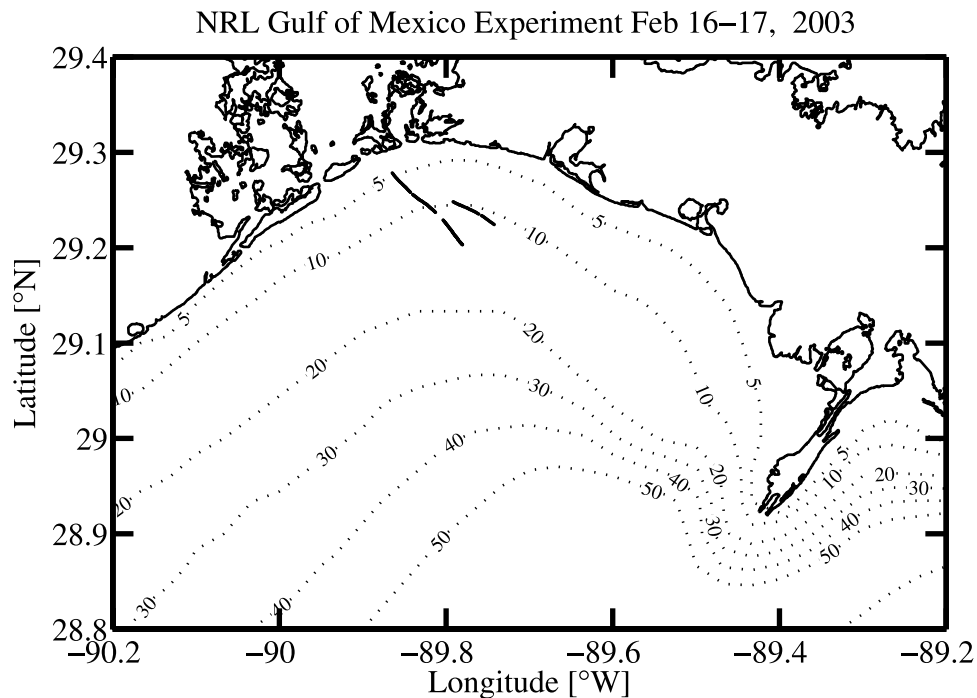
NRL Gulf of Mexico Experiment Feb 16–17, 2003

Figure 1. Location of field experiment. The solid lines show the trajectories of the wind and wave buoy off the coast of Louisiana in the Gulf of Mexico.

northwesterly (300°). The measurements were performed on 16 and 17 February, referred to as Day 1 and Day 2, respectively, in the following discussions. On each day, the buoy was deployed in the nearshore waters off the Grand Isle where the coastal line is about normal to the wind direction. The buoy free drifted southeastward following the surface current for about 7 hours before recovery. The trajectories of the drifting buoy are shown in Figure 1. The drifting velocity was estimated to be between 0.4 to 0.5 m/s. The wave field was mixed with swell generated by prefront southeasterly wind and a wind sea generated by the newly shifted northwesterly. The sensors on the buoy collected wind and wave data in bursts of 60 min long.

[10] The coordinate system for wind velocity employs the right-hand coordinate with positive U in the downwind direction and positive W in the upward direction. The sample rate was 25 Hz for the 3-D wind measurements. The WGA was sampled at 50 Hz. The sample rate of the ES parameters was 1 Hz. In the SD data acquisition, the tilting, acceleration, and pressure were sampled at 50 Hz, and the compass was sampled at 5 Hz.

2.3. Environmental Conditions

[11] Figure 2 shows the time series of the oceanic and meteorological parameters. The parameters are averaged over a 10-min period. Owing to the arrival of the cold front on Day 1, the stratification is predominantly unstable, relative humidity increases initially from 85% to 95%, U_{10} increases from 6.0 m/s to 8.3 m/s, the wind direction changes from 270° to 320°, the significant wave height (H_s) grows from 0.5 to 0.8 m, and the fetch was from around 0.5 to 15 km. After the frontal passage on Day 2, relative humidity drops to 75%, U_{10} decreases and

becomes steadier, the wind direction gradually turns northerly, H_s drops somewhat, and the fetch is from 3 to 12 km. During the entire experiment period, northwesterly and northerly winds prevail over the measurement area, and the wind sea is fetch-limited. The experimental data are separated into two categories: The first one includes the data during the cold front arrival period on Day 1 with high and increasing wind speed. The second contains those on Day 2, during which period, the air and water temperatures, wave height, and wind speed are steady.

[12] Figure 3 shows wave frequency spectra at six different timespans of 10 min each. All the frequency spectra are characterized by a double-peak structure. Figures 3a, 3b, and 3c display the frequency spectra during the period of cold front stage on Day 1, when northwesterly winds are strengthening. The swell peaks in Figures 3a, 3b, and 3c are almost constant at 0.82 rad/s (0.13 Hz), and the wind sea peaks are 2.16 rad/s (0.34 Hz), 2.20 rad/s (0.35 Hz), and 1.95 rad/s (0.31Hz), respectively. For Day 2, the wind sea peak frequencies are constant at 2.76 rad/s (0.43 Hz) (Figures 3d, 3e, and 3f). The wind speed is relatively steady (Figure 2c). The swell peak frequencies remain the same as those on Day 1.

3. Wind Stress Calculation Methods
3.1. Inertial Dissipation Method

[13] Inertial dissipation (ID) is an indirect method for wind stress computation. The method employs the high-frequency inertial subrange of the wind velocity spectrum and turbulence energy equation to obtain the wind stress. Therefore it can alleviate effects of the buoy motions on the wind stress calculation [*Fairall and Larsen*, 1986; *Edson et*
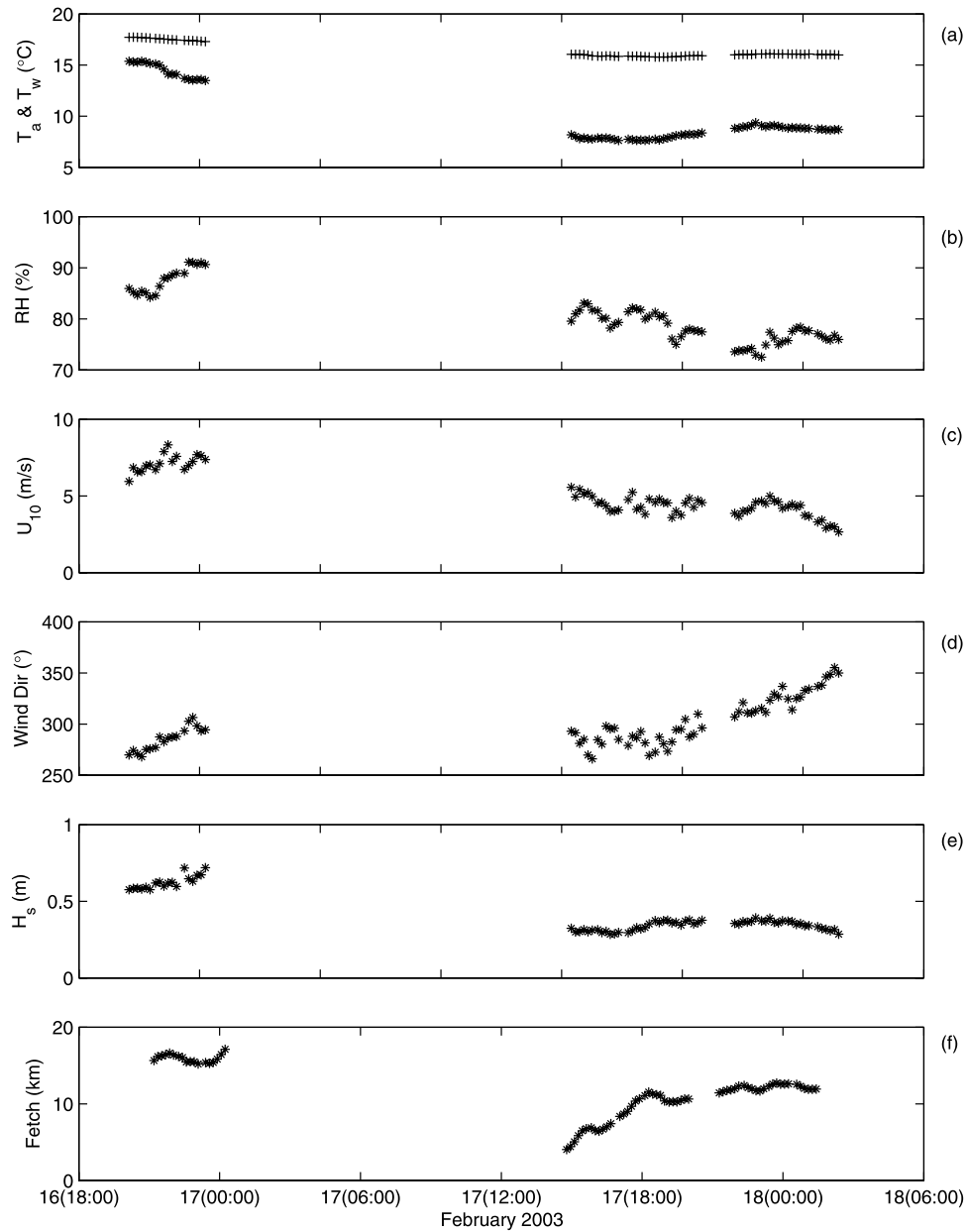
PAN ET AL.: WAVE EFFECTS ON WIND STRESS

Figure 2. Measured atmospheric and oceanic environment parameters: (a) air (plus signs) and seawater (asterisks) temperatures, (b) relative humidity, (c) 10 m wind speed, (d) wind direction, (e) significant wave height, and (f) fetch. Time shown in figure is UTC time.

al., 1991]. The method is also less sensitive to flow distortion effects than the eddy correlation method [*Fairall et al.*, 1990; *Edson et al.*, 1991].

[14] The budget equation for turbulent kinetic energy (e) is given as [*Fairall and Larsen*, 1986]

$$\overline{u'w'}\frac{\partial U}{\partial z} + \frac{\partial \left(\overline{ew'}\right)}{\partial z} + \frac{1}{\rho}\frac{\partial \overline{p'w'}}{\partial z} - \frac{g}{T}\overline{\theta'_v w'} + \varepsilon = 0, \qquad (8)$$

where u and w are along and vertical wind components, respectively; U denotes mean quantity of u; u' and w' denote turbulent terms; p' is the turbulent pressure; θ'_v is the turbulent virtual potential temperature; and ε represents dissipation rate of e. Equation (8) is rendered dimensionless by multiplying it with $\kappa z/u_*^3$. Using the Monin-Obukhov

similarity, we obtain the dimensionless energy budget equation

$$\phi(\xi) - \kappa\xi\frac{\partial\left(\overline{ew}/u_*\right)}{\partial z} - \phi_p(\xi) - \xi = \frac{\varepsilon\kappa z}{u_*^3}, \qquad (9)$$

where $\xi = z/L$. L is the Monin-Obukhov length given by

$$L = -\frac{u_*^3 T}{g\kappa\left(\overline{\theta'w'} + 0.61T\overline{q'w'}\right)}, \qquad (10)$$

where T is the air temperature in Kelvin; θ and q are potential temperature and specific humidity, respectively; θ' and q' represent the turbulent terms. In equation (9), $\phi(\xi)$ is
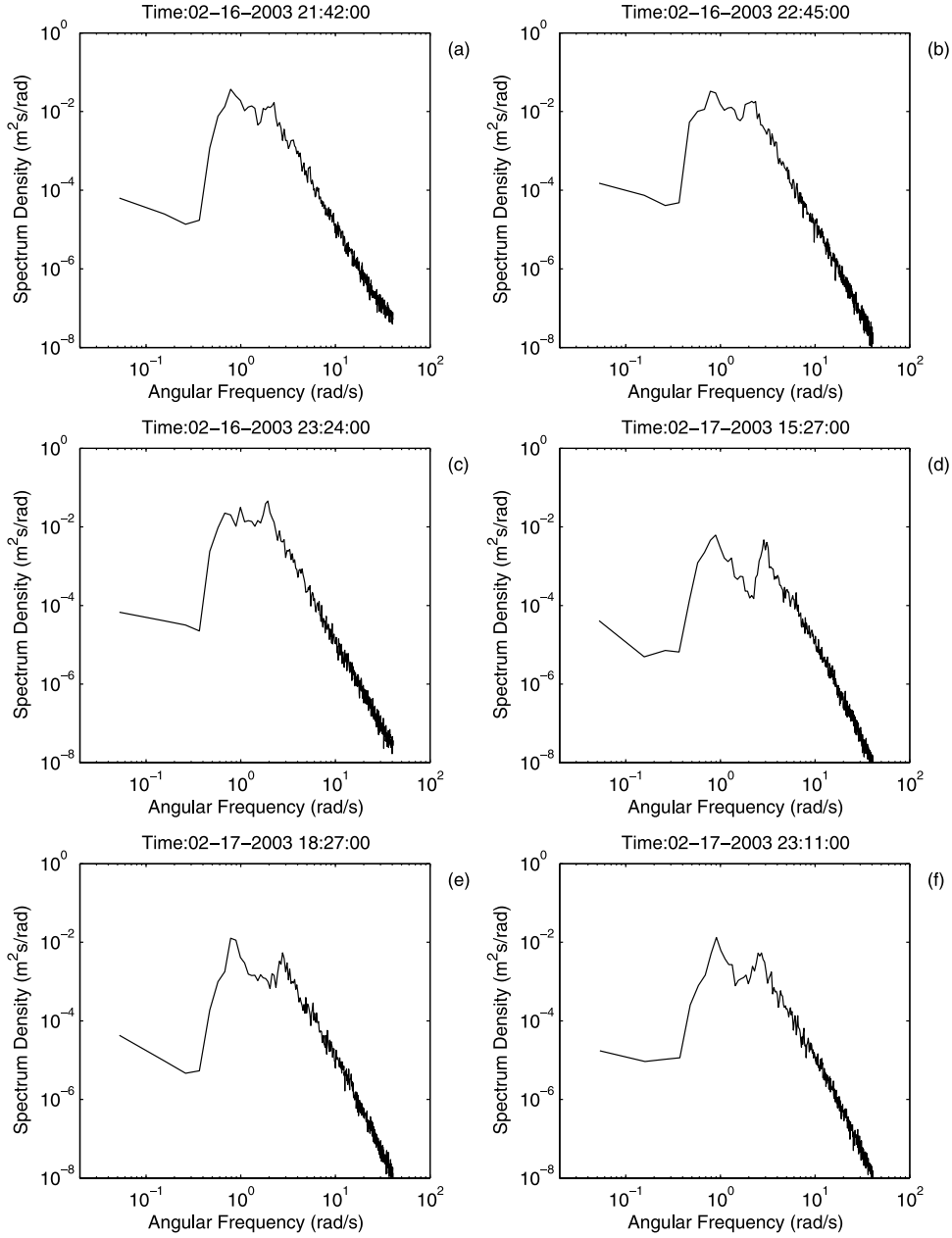
Figure 3. Frequency spectra of the surface waves in six different timespans during the experiment period. Time shown in figure is UTC time.

the dimensionless dissipation function of turbulence energy and $\phi_P(\xi)$ is the dimensionless pressure transport.

[15] Neglecting the transport terms, the dimensionless equation under the stationary condition is given by

$$\phi(\xi) - \xi = \frac{\varepsilon \kappa z}{u_*^3}, \tag{11}$$

The wind stress, sensible (H), and latent heat (E) fluxes are written as

$$\tau = -\rho \overline{u'w'}, \tag{12a}$$

$$H = \rho c_P \overline{\theta'w'}, \tag{12b}$$

$$E = \rho L_E \overline{q'w'}, \tag{12c}$$

where c_P and L_E are the specific heat of air and latent heat of evaporation of water, respectively.

[16] The dimensionless dissipation function $\phi(\xi)$ is given by [*Wyngaard and Cote*, 1971]

$$\phi(\xi) = \begin{cases} \left(1 + 0.5|\xi|^{2/3}\right)^{3/2} & \xi \leq 0 \\ \left(1 + 2.5\xi^{2/3}\right)^{3/2} & \xi > 0 \end{cases}. \tag{13}$$

The Kolmogorov variance spectrum for one-dimensional and isotropic turbulence, S_u, is related to the dissipation rate by

$$kS_u(k) = \alpha_u \varepsilon^{2/3} k^{-2/3}, \tag{14}$$

where k is the wave number, α_u is the Kolmogorov constant for variance of u, and $\alpha_u = 0.54$ [*Williams and Paulson*, 1977]. Using Taylor's hypothesis, that is, assuming "frozen" turbulence, the downstream radian wave number (k) can be replaced by $2\pi f/U$, where f is the frequency [*Large and Pond*, 1981]. Equation (14) becomes

$$S_u(k) = \alpha_u \varepsilon^{2/3} f^{-5/3} \left(\frac{U}{2\pi} \right)^{2/3}. \qquad (15)$$

[17] In this study, we use the bulk formula to calculate Monin-Obukhov length L [*Large and Pond*, 1981, 1982; *Yelland and Taylor*, 1994].

$$H = \rho c_P C_H \Delta T, \qquad (16a)$$

$$E = \rho L_E C_E \Delta q, \qquad (16b)$$

where ΔT is the temperature difference between air and seawater, and Δq represents the humidity difference between the air over sea surface and the saturated air. The Monin-Obukhov length L from equation (10) can be written as

$$L = -\frac{\rho T u_*^3}{\kappa g (H/c_P + 0.61 TE/L_E)}. \qquad (17)$$

Combining equations (11) and (17), we use iterative steps to get u_*. At the initial step, we obtain a first estimate of u_* using the bulk formula

$$u_{*(1)} = C_z^{1/2} U_z. \qquad (18)$$

Next, we calculate the first step $L_{(1)}$ based on equations (16) and (17). We then solve equation (11) to obtain the second step $u_{*(2)}$. The convergent solution of u_* can be obtained in six iterations.

[18] We use the least squares fit to obtain the dissipation rate in the wind inertial subrange (2–12.5 Hz) shown in Figure 4. The bulk coefficients are selected as $C_E = 1.15 \times 10^{-3}$, and $C_H = 1.13 \times 10^{-3}$ [*Large and Pond*, 1982]. At the initial step for calculating $u_{*(1)}$, C_z is 1.2×10^{-3} [*Large and Pond*, 1981]. We calculate the wind stress every 10 min. A total of 72 wind stresses (represented by u_*) are generated from 12 hours of field data obtained over the 2 days.

3.2. Eddy Correlation Method

[19] The eddy correlation (EC) is a direct method for calculating the wind stress. The along-wind stress is given as

$$\tau = -\rho \overline{u'w'}. \qquad (19)$$

where u' and w' are relative to the Earth coordinate system. However, in this study, the wind measurements were made on a moving coordinate system, namely, the buoy frame system. In order to obtain wind data relative to the Earth system, we have to correct buoy motion effects on the measured wind velocity. On the basis of an approach by *Fujitani* [1981], *Anctil et al.* [1994] and *Edson et al.* [1998] developed an algorithm for buoy motion effect corrections.

Their motion correction method is employed in this study. The corrected wind velocity is expressed as

$$\mathbf{V_{CR}} = \mathbf{T_{BE}V_{OB}} + \mathbf{\Omega} \times \mathbf{T_{BE}L_B} + \mathbf{T_{BE}V_a}, \qquad (20)$$

where $\mathbf{V_{CR}}$ is the corrected wind velocity; $\mathbf{V_{OB}}$ represents the observed wind velocity in buoy platform; $\mathbf{T_{BE}}$ is the transform matrix from buoy platform coordinate to the Earth reference coordinate, and is a function of buoy tilting angles, pitch, roll, and yaw; $\mathbf{\Omega}$ is the angular velocity vector of the buoy coordinate system; $\mathbf{L_B}$ is the position vector of the wind sensor with respect to the motion sensor; and $\mathbf{V_a}$ is the buoy velocity vector relative to the buoy coordinate system.

[20] The first term of the right-hand side of equation (20) ($\mathbf{T_{BE}V_{OB}}$) represents the conversion of the anemometer measurements to the Earth system using the transform matrix. The second term ($\mathbf{\Omega} \times \mathbf{T_{BE}L_B}$) accounts for the angular velocities induced by the buoy's rotations. The third term compensates the axial motions of the buoy. This is done by measuring linear accelerometer signals and integrating them into velocities.

[21] After this processing, the covariance of the turbulent u and w is computed to produce a time series of EC wind stresses. The timespan of each segment is 10 min, the same as that of the ID wind stresses.

4. Results and Analysis

4.1. Wind Stress

[22] Figure 5a illustrates the time series of the stability parameter (ξ). During the cold front arrival period with strong winds on Day 1, the stability condition is near neutral. On the second day, the condition is unstable due to decreased winds and increased air-sea temperature difference. Figure 5b displays the computed wind stresses from ID and EC methods with time. The EC wind stress is usually greater than the ID stress. A further comparison between the two wind stress estimates is given as a scatterplot of u_*^2 (ID) versus $-\overline{u'w'}$ (EC), shown in Figure 6. Figure 6 reveals that a bias exists between the two kinds of wind stress. *Donelan et al.* [1997] found that in the presence of the cross and counter swell, the ID method underestimates wind stress as compared with the EC method, but in the pure wind sea cases, the two methods give consistent results. The wind stress data by *Donelan et al.* [1997] in the counter swell condition are also shown in Figure 6 as triangles. The wind stresses of this study are consistent with the data by *Donelan et al.* [1997] when u_*^2 is less than 0.07 m^2/s^2. In the higher u_*^2 range, Donelan's data indicate that ID wind stress is larger than EC wind stress, whereas this study shows that even in higher u_*^2 range ($u_*^2 > 0.07$ m^2/s^2), the ID wind stress is still smaller than the EC wind stress.

[23] *Donelan et al.* [1997] gave an explanation to this phenomenon. The ID method depends on the assumptions of steady state and similarity of cascade of energy from scales of input to scales of dissipation. The presence of swell leads to a narrowbanded energy transfer (input) in addition to the broadbanded self-similar transfer due to roughness of the shorter wind spectrum. The ID method responds only to the turbulent Reynolds stress through its interaction with the wind profile. In the presence of long
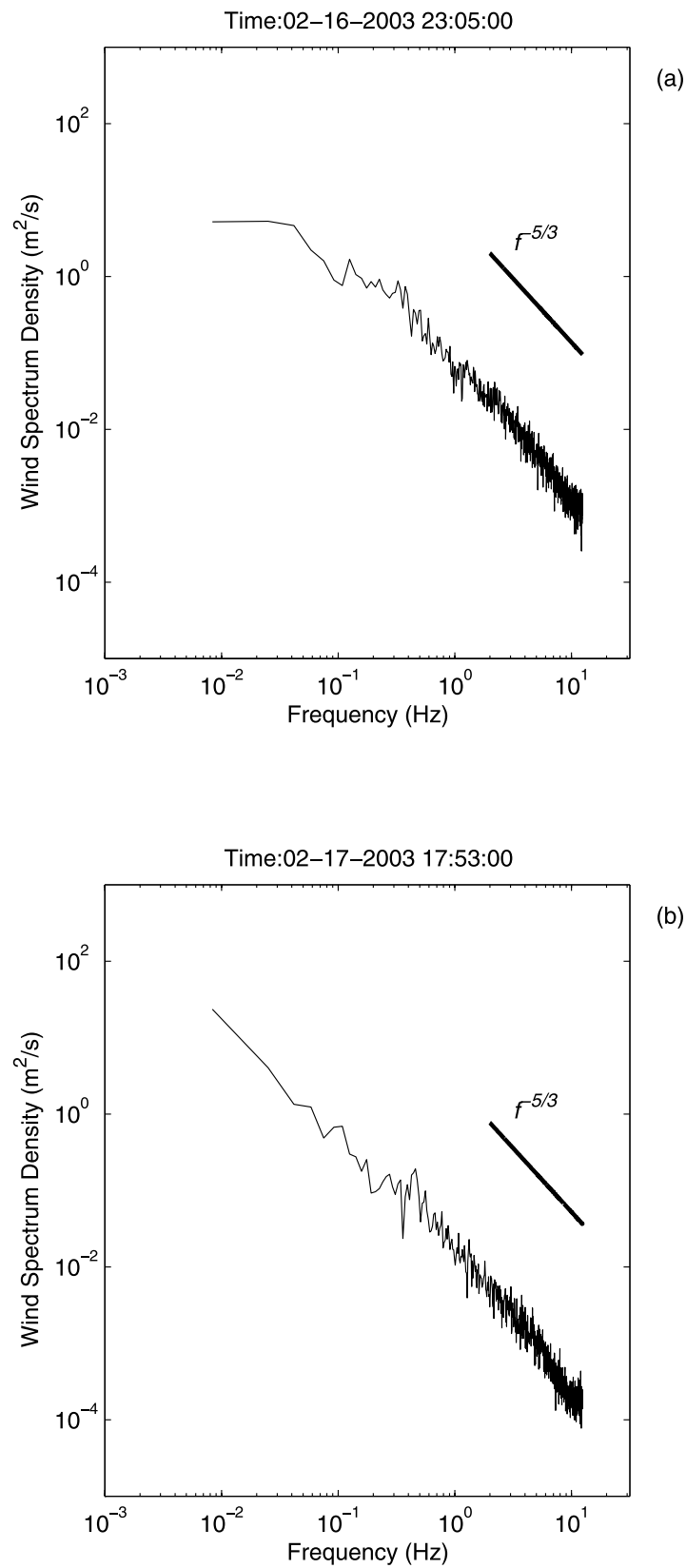
Figure 4. Turbulent spectra of the along-wind velocity at (a) 2305 UTC 16 February and (b) 1753 UTC 17 February. The solid lines in Figures 4a and 4b represent $f^{-5/3}$.
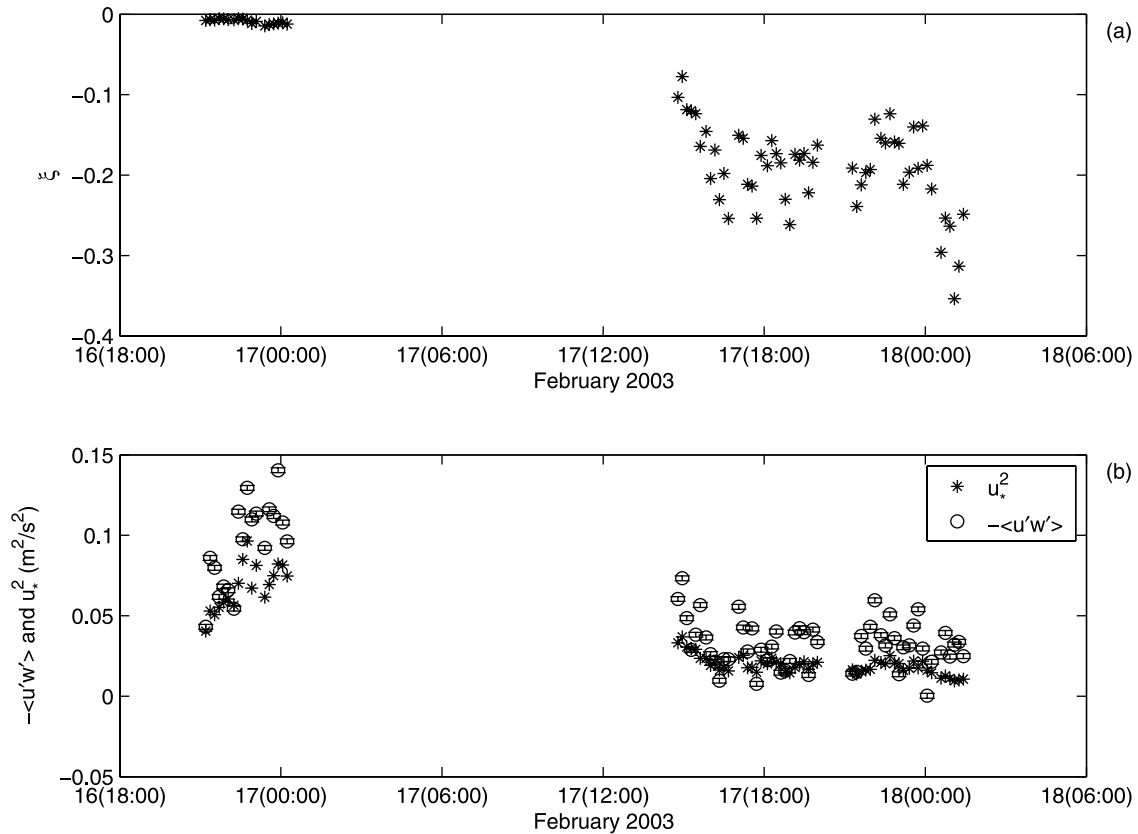
Figure 5. Wind stress calculation results: (a) the stability parameter $\xi (= z/L)$, in which L is the Monin-Obukhov length and z is the measurement height, and (b) inertial dissipation (u_*^2) and eddy correlation ($-\langle u'w' \rangle$) wind stresses with time. (In the figure, $-\langle u'w' \rangle$ represents $-\overline{u'w'}$ in the text.) The error bars represent motion correction residual errors. Time shown in figure is UTC time.

waves (swell), some fraction of wind stress is carried by wave-coherent and nonturbulent components. These tend to cause a reduction on the slope of the wind profile that is more pronounced near the surface. The ID method, dependent on the production of kinetic energy through the interaction of the turbulent stress with the wind profile, may underestimate the total stress [*Donelan and Dobson*, 2001]. The applicability of the dissipation method in swell situations injects large-scale energy within a narrow range of scales and may not explain the cascade of energy to the smaller scales.

[24] With lower observation height than the previous studies (Table 1), this study supports the result by *Donelan et al.* [1997]. *Drennan et al.* [1999b] observed that turbulence levels in the inertial subrange are similar for pure wind sea and swell runs of similar wind speed. It is impossible to recover the swell-generated wind stress using the high-frequency range of the wind spectrum, because the swell introduces an additional length scale into the problem. The wind stress carried by swell cannot be modeled by the Monin-Obukhov theory.

4.2. Swell-Related Drag Coefficient

[25] On the basis of the wind stresses computed by ID and EC methods, we calculated the neutral drag coefficients, which are referred to as C_{10} (ID) and C_{10} (EC), respectively, and plotted against U_{10} in Figure 7. Comparisons of the

drag coefficients with those from several earlier studies are also given in Figure 7. Table 1 lists the regression formulae and data descriptions of the earlier studies [*Smith*, 1980; *Large and Pond*, 1981; *Smith*, 1988; *Dobson et al.*, 1994; *Drennan et al.*, 1999a; *Donelan et al.*, 1997].

[26] Figure 7 shows that C_{10} (ID) is consistent with the drag coefficients under the pure wind sea condition by *Drennan et al.* [1999b] and *Donelan et al.* [1997], and also consistent with the ID wind stresses reported by *Large and Pond* [1981] and *Dobson et al.* [1994] in the mixed sea condition. In applying the inertial dissipation method, it is assumed that wind stress is constant in the whole ocean boundary layer, so the ID wind stress is supposed to be independent of the measurement height. The EC method in principle resolves the total wind stress under mixed sea conditions. The swell-induced wind stress is more pronounced near the surface [*Donelan and Dobson*, 2001]. Hence it is reasonable that the lower level measurements in this study recover more of the wave-induced wind stress and drag coefficient. Least squares regression of the C_{10} (EC) in the presence of the counter swell yields

$$C_{10} =$$
$$\begin{cases} 10^{-3}\left(52.13/U_{10}^2 - 16.96/U_{10} + 2.82\right) & 3.0 < U_{10} \leq 6.0 \text{ m/s} \\ 10^{-3}\left(0.26U_{10} - 0.14\right) & 6.0 < U_{10} < 8.3 \text{ m/s} \end{cases},$$
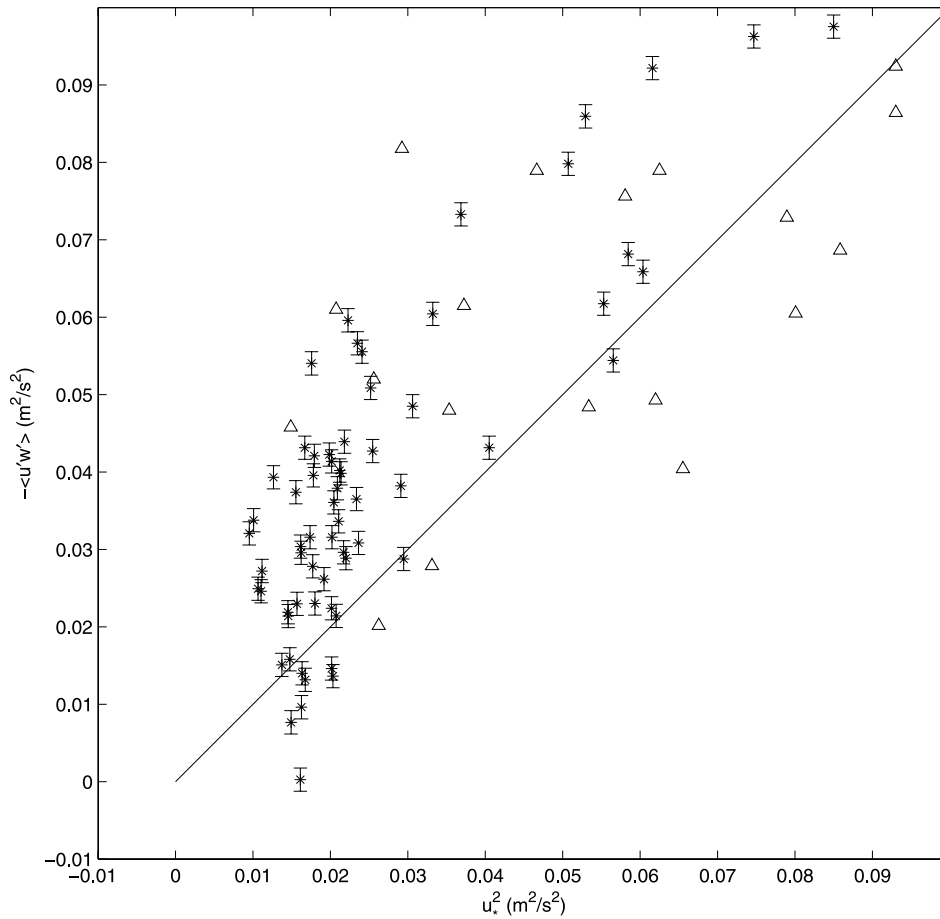
$$\tag{21}$$

Figure 6. Scatterplot of $-\langle u'w' \rangle$ and u_*^2, in which asterisks represent results of this study and triangles denote the data by *Donelan et al.* [1997] under the counter swell condition. The error bars represent motion correction residual errors.

which is shown in Figure 7 as the thick dotted line. The regression coefficient r has a low value of 0.55 because of the large scatter of the data. The result suggests that when $U_{10} < 6.0$ m/s, the swell effect may be a dominant factor for the wind stress with mixed sea state of the counter-wind swell.

[27] In this study, on the basis of the previous analysis, we use the difference between the wind stresses of the eddy correlation and inertial dissipation to represent swell-induced wind stress,

$$\frac{\tau_{swell}}{\rho} = \left(-\overline{u'w'} \right) - u_*^2, \tag{22}$$

where $-\overline{u'w'}$ represents the EC wind stress, and u_*^2 represents ID stress. The swell-related drag coefficient (ΔC_{10}) is defined as the difference between the drag coefficient with and without swell, and can be derived from the swell-induced wind stress as

$$\Delta C_{10} = \frac{\tau_{swell}}{\rho U_{10}^2}. \tag{23}$$

[28] *Donelan and Dobson* [2001] suggested that the swell-related drag coefficient might be related to the swell steepness, a geometric parameter of the swell. *Dobson et al.*

Table 1. Drag Coefficient Regressions and Data From This and Earlier Studies

| Study	$1000C_{10}$	U_{10}, m/s	Anemometer	Sensor Height, m
Smith [1980]	$0.61 + 0.63U_{10}$	$6-22$	thrust	13.4
Large and Pond [1981]	$0.49 + 0.065U_{10}$	$11-25$	K Gill propeller	12.5
	1.2	$4-11$		
Smith [1988]	$z_0 = \alpha u_*^2/g + 0.11\nu/u_*$			
Dobson et al. [1994]	$0.72 + 0.061U_{10}$	$5-18$	K Gill propeller	14
Donelan et al. [1997]	C_{10} data under wind sea and		K Gill propeller	12
	counter swell conditions	$3-14$		
Drennan et al. [1999a]	$0.60 + 0.07U_{10}$	$6-14$	K Gill propeller	5
This study	$52.13/U_{10}^2 - 16.96/U_{10} + 2.82$	$3-6$	ultrasonic	1.5
	$0.26U_{10} - 0.14$	$6-8.3$		
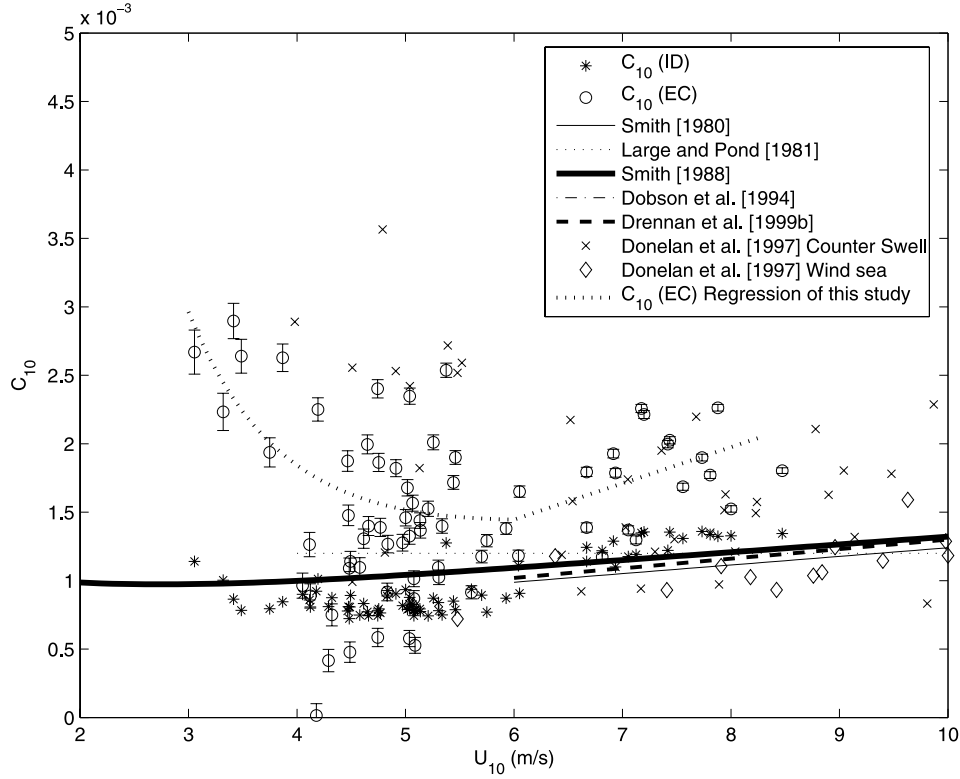
Figure 7. Neutral drag coefficients (C_{10}) calculated by the ID (asterisks) and EC (open circles) methods versus U_{10}. Also shown are C_{10} data of *Donelan et al.* [1997] under pure wind sea (diamonds) and counter swell (crosses) conditions, and C_{10} regressions of earlier studies. The error bars represent motion correction residual errors.

[1994] used a method to separate the swell and wind-sea wave signals. Following this method, we filter out the wind sea amplitude and obtain the swell elevation, the swell significant wave height (H_s), and the swell steepness (k_pH_s), in which k_p is the swell peak wave number. (Hereinafter, H_s, k_p, and C_p are used to represent swell parameters.) The kinematic property of the swell can be a factor affecting the air-sea momentum interaction. In this study, we use the ratio of the wind speed and the swell peak phase (U_{10}/C_p, in which, C_p is the peak phase speed of the swell) to describe the kinematic property of the swell. These geometric and kinematic parameters reflect the physical property of the swell. In the following, we seek to establish the empirical relationship between the swell-related drag coefficient and the geometric and kinematic parameters.

[29] Figure 8a shows the relationships between ΔC_{10} and k_pH_s in U_{10}/C_p ranges between 0.45 and 0.55 and between 0.55 and 0.65. The data in these ranges are chosen because of the larger data population and less data scatter (Figure 8c). Figure 8a reveals that the swell-related ΔC_{10} is proportional to the swell steepness (k_pH_s). In U_{10}/C_p ranges between 0.45 and 0.55, the regression result is $\Delta C_{10} = 1.33(k_pH_s)^{2.0}$, and between 0.55 and 0.65, it is $\Delta C_{10} = 0.038(k_pH_s)^{1.1}$. In order to determine the relationship between ΔC_{10} and U_{10}/C_p after removing the effect of k_pH_s variation, ΔC_{10} data are examined in k_pH_s ranges between 0.018 and 0.021, and between 0.021 and 0.024 (Figure 8b). Figure 8b reveals that ΔC_{10} is inversely proportional to U_{10}/C_p. In the k_pH_s range between 0.018 and 0.021, the regression between ΔC_{10} and U_{10}/C_p is

$\Delta C_{10} = 3.83 \times 10^{-5}(U_{10}/C_p)^{-3.2}$, and for k_pH_s range between 0.021 and 0.024, it is $\Delta C_{10} = 1.99 \times 10^{-4}(U_{10}/C_p)^{-2.2}$. We choose the swell steepness to scale the swell-related drag coefficient, and try to find the relationship between ΔC_{10} and U_{10}/C_p. On the basis of the regression formulae between ΔC_{10} and k_pH_s, we use $(k_pH_s)^{1.6}$, the geometric mean of the regression formulae $(k_pH_s)^{1.1}$ and $(k_pH_s)^{2.0}$ in Figure 8a, to scale ΔC_{10}. The relationship between $\Delta C_{10}/(k_pH_s)^{1.6}$ and U_{10}/C_p is shown in Figure 8c. The following regression formula is obtained:

$$\Delta C_{10} = 5.1 \times 10^{-2} \frac{(k_pH_s)^{1.6}}{(U_{10}/C_p)^{2.6}}. \qquad (24)$$

Data points with negative τ_{swell} are excluded in the regression analysis. The regression coefficient r is 0.71. Equation (24) suggests that the swell-related drag coefficient is proportional to the swell steepness and inversely proportional to the ratio of wind speed and swell peak phase speed. The regression formula, equation (24), is shown in Figure 8c by a solid line. The solid circles are $\Delta C_{10}/(k_pH_s)^{1.6}$ bin-averaged with 0.1 intervals for U_{10}/C_p from 0.3 to 1.0. The error bars represent the standard deviations of $\Delta C_{10}/(k_pH_s)^{1.6}$ in these intervals.

5. Error Analysis

[30] The ID method employs the high-frequency subrange of the along-wind spectrum, and therefore it alleviates
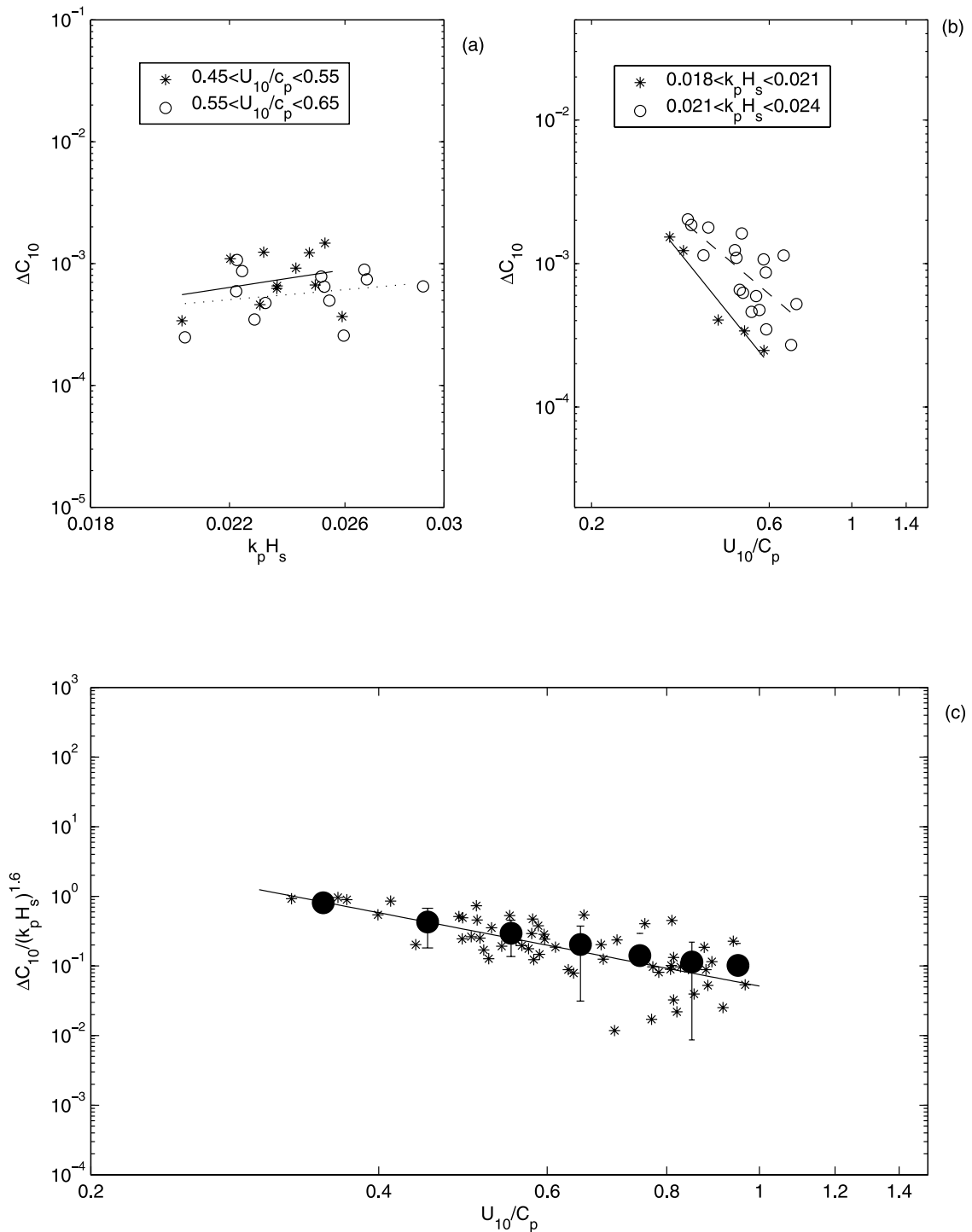
Figure 8. (a) Swell-related drag coefficients (ΔC_{10}) versus the swell steepness $k_p H_s$ in U_{10}/C_p ranges between 0.45 and 0.55 (asterisks) and between 0.55 and 0.65 (open circles), where C_p is the swell peak phase speed. The solid line is $\Delta C_{10} = 1.33(k_p H_s)^{2.0}$, and the dashed line is $\Delta C_{10} = 0.038(k_p H_s)^{1.1}$. (b) ΔC_{10} versus U_{10}/C_p in $k_p H_s$ ranges between 0.016 and 0.021 (asterisks), and between 0.021 and 0.024 (open circles). The solid line is $\Delta C_{10} = 3.83 \times 10^{-5}(U_{10}/C_p)^{-3.2}$. The dashed line is $\Delta C_{10} = 1.99 \times 10^{-4}(U_{10}/C_p)^{-2.2}$. (c) The relationship between $\Delta C_{10}/(k_p H_s)^{1.6}$ and U_{10}/C_p, in which the straight line represents $\Delta C_{10} = 5.2 \times 10^{-2} (k_p H_s)^{1.6} (U_{10}/C_p)^{-2.6}$ with a regression coefficient $r = 0.71$. The solid circles denote the average of $\Delta C_{10}/(k_p H_s)^{1.6}$ in every 0.1 interval of U_{10}/C_p from 0.3 to 1.0. The error bars represent the standard deviations of $\Delta C_{10}/(k_p H_s)^{1.6}$ in these intervals.

the effects of the buoy motion including the buoy accelerations and orbital motions on the wind measurements. Using the EC method, we need to correct the buoy motion effects on the anemometer measurements in the buoy coordinate system. Theoretically, after motion correction, the wind data should be free of the buoy motions. However, measurement errors of the motion sensors could cause residual errors. These errors might contaminate EC wind stress calculations. It is necessary to give an error analysis to the motion correction to verify that these residual errors could not affect the results of this study.

[31] A standard error analysis approach is employed in this study [Fristchen and Gay, 1979; Edson et al., 1991]. The error in some unspecified property $G(x_1, x_2, \cdots, x_n)$ is expressed in terms of errors δx_1, δx_1, $\cdots$, δx_n.

$$\Delta G = \frac{\partial G}{\partial x_1}\Delta x_1 + \frac{\partial G}{\partial x_2}\Delta x_2 + \cdots + \frac{\partial G}{\partial x_n}\Delta x_n. \quad (25)$$

If x_1, x_2, $\cdots$, and x_n are independent variables and the errors in x_1, x_2, $\cdots$, and x_n are uncorrelated, the most probable error is the sum of the squares of the individual terms,

$$|\Delta G|_{\max} = \left[\left(\frac{\partial G}{\partial x_1}\right)^2 \Delta x_1^2 + \left(\frac{\partial G}{\partial x_2}\right)^2 \Delta x_2^2 + \cdots + \left(\frac{\partial G}{\partial x_n}\right)^2 \Delta x_n^2\right]^{1/2}. \quad (26)$$

On the basis of these error formulae, the errors in equation (20) can be derived as

$$
\begin{aligned}
\Delta\mathbf{V_{CR}} = &\left(\frac{\partial\mathbf{T_{BE}}}{\partial\theta}\mathbf{V_{OB}} + \frac{\partial\mathbf{\Omega}}{\partial\theta}\times\mathbf{T_{BE}L_B}\right.\\
&\left. + \mathbf{\Omega}\times\frac{\partial\mathbf{T_{BE}}}{\partial\theta}\mathbf{L_B} + \mathbf{V_a}\frac{\partial\mathbf{T_{BE}}}{\partial\theta}\right)\Delta\theta\\
&+\left(\frac{\partial\mathbf{T_{BE}}}{\partial\phi}\mathbf{V_{OB}} + \frac{\partial\mathbf{\Omega}}{\partial\phi}\times\mathbf{T_{BE}L_B}\right.\\
&\left. + \mathbf{\Omega}\times\frac{\partial\mathbf{T_{BE}}}{\partial\phi}\mathbf{L_B} + \mathbf{V_a}\frac{\partial\mathbf{T_{BE}}}{\partial\phi}\right)\Delta\phi\\
&+\left(\frac{\partial\mathbf{T_{BE}}}{\partial\psi}\mathbf{V_{OB}} + \frac{\partial\mathbf{\Omega}}{\partial\psi}\times\mathbf{T_{BE}L_B}\right.\\
&\left. + \mathbf{\Omega}\times\frac{\partial\mathbf{T_{BE}}}{\partial\psi}\mathbf{L_B} + \mathbf{V_a}\frac{\partial\mathbf{T_{BE}}}{\partial\psi}\right)\Delta\psi + \mathbf{T_{BE}}\Delta\mathbf{V_a}, \quad (27)
\end{aligned}
$$

where θ, ϕ, and ψ represent pitch, roll, and yaw. Let

$$
\begin{aligned}
\Delta u &= \beta_{u,\theta}\Delta\theta + \beta_{u,\phi}\Delta\phi + \beta_{u,\psi}\Delta\psi + \beta_{u,u}\Delta u_a\\
\Delta w &= \beta_{w,\theta}\Delta\theta + \beta_{w,\phi}\Delta\phi + \beta_{w,\psi}\Delta\psi + \beta_{w,w}\Delta w_a
\end{aligned}, \quad (28)
$$

where $\beta_{u,\theta}$, $\beta_{u,\phi}$, $\beta_{u,\psi}$, and $\beta_{u,u}$ represent the coefficients of $\Delta\theta$, $\Delta\phi$, $\Delta\psi$, and $\Delta\mathbf{V}_a$ in equation (27) for along-wind (u) component, respectively, and $\beta_{w,\theta}$, $\beta_{w,\phi}$, $\beta_{w,\psi}$, and $\beta_{w,w}$ denote the coefficients of $\Delta\theta$, $\Delta\phi$, $\Delta\psi$, and $\Delta\mathbf{V}_a$ in equation (27) for vertical-wind (w) component, respectively. Therefore the most probable errors for u and w are given by

$$
\begin{aligned}
\overline{|\Delta u|}_{\max} &= \left(\beta_{u,\theta}^2\Delta\theta^2 + \beta_{u,\phi}^2\Delta\phi^2 + \beta_{u,\psi}^2\Delta\psi^2 + \beta_{u,u}^2\Delta u_a^2\right)^{1/2}\\
\overline{|\Delta w|}_{\max} &= \left(\beta_{w,\theta}^2\Delta\theta^2 + \beta_{w,\phi}^2\Delta\phi^2 + \beta_{w,\psi}^2\Delta\psi^2 + \beta_{w,w}^2\Delta w_a^2\right)^{1/2}.
\end{aligned} \quad (29)
$$

Figure 9 shows the most probable errors of u and w calculated using equation (29) for this study. The left panel shows the error in the first period and the right panel shows that in the second period. It can be seen that most Δu (top panel) is less than 0.0025m/s, and most Δw is less than 0.0012m/s. If we consider errors for u and w, the eddy correlation wind stress formula is changed as

$$
\begin{aligned}
\overline{(u - \bar{u})(w - \bar{w})} &= \overline{(u' + \tilde{u} + \Delta u)(w' + \tilde{w} + \Delta w)}\\
&= \overline{u'w'} + \overline{\tilde{u}\tilde{w}} + \overline{\tilde{u}\Delta w} + \overline{\tilde{w}\Delta u} + \overline{\Delta u\Delta w}, \quad (30)
\end{aligned}
$$

where $\tilde{u}$ and $\tilde{w}$ are the wave coherent components. The last three terms of equation (30) represent the residual errors associated with the motion correction. These terms can be derived as

$$\overline{\tilde{u}\Delta w} + \overline{\tilde{w}\Delta u} + \overline{\Delta u\Delta w} \leq \overline{|\tilde{u}|}|\Delta w|_{\max} + \overline{|\tilde{w}|}|\Delta w|_{\max} + |\Delta u|_{\max}|\Delta w|_{\max}. \quad (31)$$

As revealed in Figure 9, $\overline{|\Delta u|}_{\max}$ and $\overline{|\Delta w|}_{\max}$ could be 0.0025 m/s and 0.0012 m/s, respectively. In order to analyze the errors, we need to estimate the values of $\overline{|\tilde{u}|}$ and $\overline{|\tilde{w}|}$ by using equation (31). We calculate the means of the absolute values of total u and w fluctuations, namely $\overline{|u - \bar{u}|}$ and $\overline{|w - \bar{w}|}$. They are 0.64 and 0.27 m/s, respectively. Actually, magnitudes of the wave-related wind components are less than total fluctuation magnitudes. Here $\overline{|\tilde{u}|}$ and $\overline{|\tilde{w}|}$ are replaced by the values of $\overline{|u - \bar{u}|}$ and $\overline{|w - \bar{w}|}$. Therefore we have $\overline{|\tilde{u}|}|\Delta w|_{\max} = 0.00077$ m²/s², $\overline{|\tilde{w}|}|\Delta u|_{\max} = 0.00068$ m²/s², and $|\Delta u|_{\max}|\Delta w|_{\max} = 0.000003$ m²/s². The total of the three terms is 0.0015 m²/s². Here the most probable error estimation method is used; the actual error is less than this amount. We added error bars of ±0.0015 m²/s² to Figures 5b and 6. Figure 5b suggests that the residual wind stress error after motion correction is small. The average of $-\overline{u'w'}$ is 0.048, and the error is just 2.9% of the mean. As shown in Figure 6, we can see that even if the errors are taken into account, most of EC wind stresses are larger than ID stresses. The residual error does not affect the result. The C_{10} errors are calculated based on the wind stress error, and are shown in Figure 7 as error bars. Figure 7 indicates that the residual C_{10} errors are very much smaller than the deviations of the C_{10} itself. We calculate the mean of the deviations of C_{10} in every 1.0 m/s interval between 3.0 and 8.0 m/s, and the mean is 0.42×10^{-3}. However, the mean of the C_{10} error is calculated as 0.05×10^{-3}, which is much less than the C_{10} deviation. This analysis suggests the motion correction residual error does not affect the result of this study.

6. Flow Distortion

[32] Flow distortion may affect wind velocity measurements for some wind sensors. In order to overcome this problem, new types of wind sensors are improved in the structure design. The YOUNG Model 81000 ultrasonic anemometer used in this study is one of these improved design sensors. The anemometer has three opposing pairs of ultrasonic transducers, and it is like two wind sensors placed
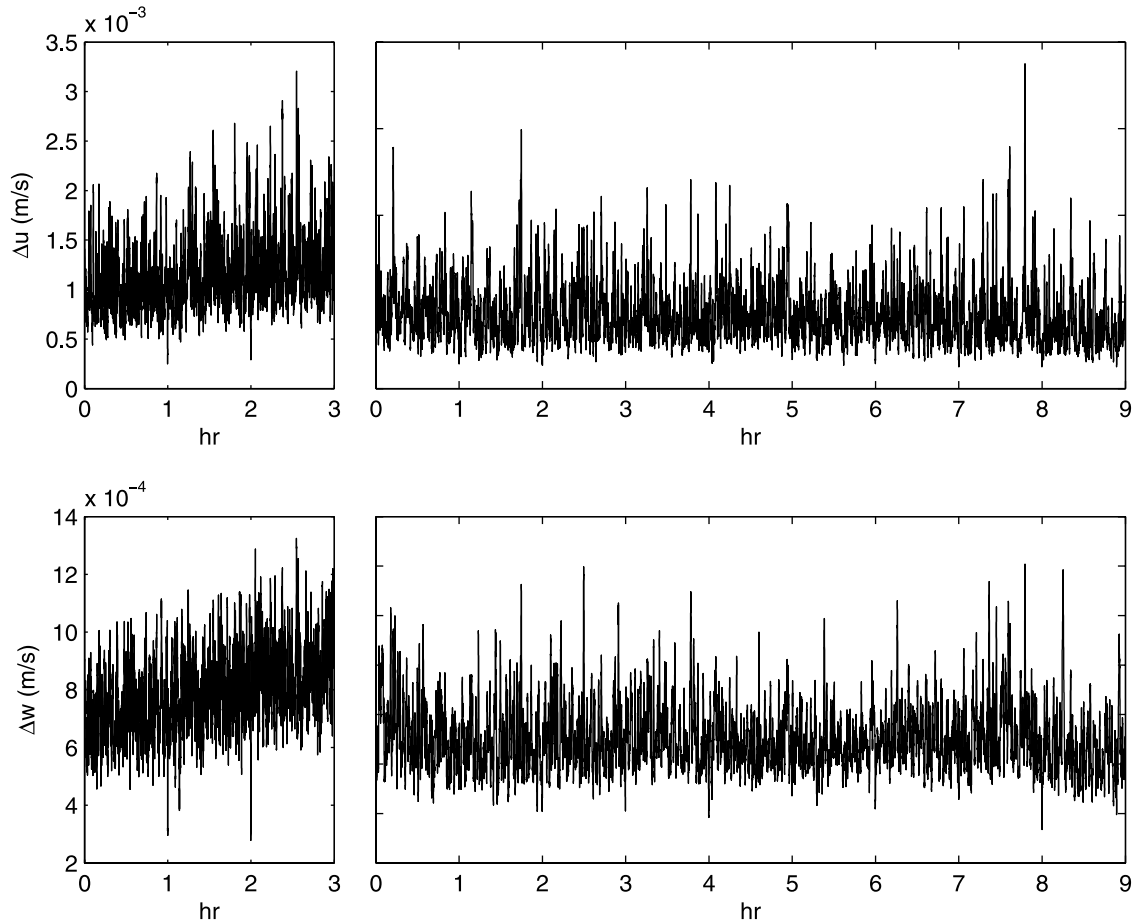
Figure 9. Most probable residual errors for (top) along-wind u and (bottom) vertical wind w. (left) Error in the first phase and (right) error in the second phase.

upward and downward, respectively. This design could minimize the flow distortion effects. On the basis of *Wyngaard*'s [1981] flow distortion theory, *Edson et al.* [1991] analyzed the flow distortion effects on the wind measurements using two sonic anemometers which were mounted upward and downward on a mast. Their results show that when combining the two anemometer wind measurements, the calculated drag coefficient only has a 5.1% difference from that after flow distortion correction. In our case, the scatter of the EC drag coefficient is 27%. This is much greater than the flow distortion uncertainty. In addition, the YOUNG 81000 ultrasonic anemometer used in this study was wind tunnel tested and calibrated to compensate for flow distortion effects of the support structure. All this suggests that the flow distortion is not important in this study.

7. Discussions

[33] The difference between the ID and EC wind stresses reflects swell impacts. Considering that the along-and vertical-wind velocities are decomposed as

$$u = U + u' + u_s \tag{32a}$$

$$w = W + w' + w_s, \tag{32b}$$

where u_s and w_s represent the swell-related wind components. Using the EC method, we obtain the wind stress by computing the covariance of u and w fluctuation components,

$$\overline{(u - U)(w - W)} = \overline{(u' + u_s)(w' + w_s)}. \tag{33}$$

We assume that the turbulent and swell terms are uncorrelated with each other. Therefore the EC wind stress can be derived as

$$\tau(EC) = -\rho\overline{(u - U)(w - W)} = -\rho\overline{u'w'} - \rho\overline{u_s w_s}. \tag{34}$$

where $-\rho\overline{u_s w_s}$ represents the swell-contributed wind stress. This suggests that the EC wind stress includes the swell-related component.

[34] In the presence of swell, *Donelan and Dobson* [2001] concluded that there is a reduction in wind profile near the ocean surface. *Drennan et al.* [1999b] believed that Monin-Obukhov similarity theory does not hold because of the presence of swell. On the basis of these two points, we give a theoretical analysis for the inertial dissipation wind stress. Because the swell-induced wind exists over the

surface layer, and if we neglect the transport and pressure terms, equation (8) is changed to

$$\overline{u'w'}\frac{\partial U}{\partial z} + \left(\overline{u'w'} + \overline{u_s w_s}\right)\frac{\partial U_s}{\partial z} + \overline{u_s w_s}\frac{\partial U}{\partial z}$$
$$- \frac{g}{T}\overline{\theta'_v w'} - \frac{g}{T}\overline{\theta_{vs} w_s} + \varepsilon = 0, \tag{35}$$

where U_s represents the swell-induced average velocity and θ_{vs} denotes the swell-related potential temperature. Multiplication of the equation with $\kappa z/u_*^3$ yields a dimensionless energy balance equation,

$$\kappa z\frac{\partial U}{\partial z}/u_* - \kappa z\left(\overline{u'w'} + \overline{u_s w_s}\right)\frac{\partial U_s}{\partial z}/u_*^3 - \kappa z\overline{u_s w_s}\frac{\partial U}{\partial z}/u_*^3$$
$$+ \frac{\kappa z g}{T}\overline{\theta'_v w'}/u_*^3 + \frac{\kappa z g}{T}\overline{\theta_{vs} w_s}/u_*^3 - \frac{\varepsilon\kappa z}{u_*^3} = 0 \tag{36}$$

We apply Monin-Obukhov similarity theory to the pure wind turbulence terms, and therefore we have

$$\phi_u(\xi) - \xi - \left[\kappa z\left(\overline{u'w'} + \overline{u_s w_s}\right)\frac{\partial U_s}{\partial z}/u_*^3\right.$$
$$\left. + \kappa z\overline{u_s w_s}\frac{\partial U}{\partial z}/u_*^3 - \frac{\kappa z g}{T}\overline{\theta_{vs} w_s}/u_*^3\right] = \frac{\varepsilon\kappa z}{u_*^3}. \tag{37}$$

We use a symbol, Ξ_s, to represent the swell-related terms in equation (37); a simplified equation is given by

$$\phi_u(\xi) - \xi - \Xi_s = \frac{\varepsilon\kappa z}{u_*^3}. \tag{38}$$

Comparing equation (11) with equation (38), we can see that equation (11) used for calculation of the wind stress does not include the swell-related terms. In the presence of swell it forces the swell-related term (Ξ_s) to become zero using equation (11), and thus the inertial dissipation method based on equation (11) cannot capture the swell-induced wind stress.

8. Summary

[35] Wind and wave data were measured in a field experiment during a period of cold front passage. The sea state is mixed by counter swell and wind sea under the fetch-limited condition. The buoy measurements include 3-D wind components, wave, and other air-sea environmental parameters. The wind sensor height is 1.5 m above the sea surface, which is favorable for capturing more wave-induced wind stress component. We apply two methods to compute the wind stress: the inertial dissipation (ID) and the eddy correlation (EC). The motion correction is applied to the 3-D wind data in using the EC method. Under the fetch-limited experimental condition, the ID wind stress is less than that from the EC method, which is consistent with the results of *Donelan et al.* [1997] and *Drennan et al.* [1999b] with a clearer signature of swell influence. The wind stress difference between the two methods is empirically related to the swell parameters. The result (equation (24)) suggests that the swell-related drag coefficient (ΔC_{10}), the difference between the drag coefficient with and without swell, is proportional to the

swell steepness and inversely proportional to the ratio of the wind speed and the swell peak phase speed.

References

Anctil, F., and M. A. Donelan (1996), Air-water momentum flux observations over shoaling waves, *J. Phys. Oceanogr.*, *26*, 1344–1353.

Anctil, F., M. A. Donelan, and W. M. Drennan (1994), Eddy-correlation measurements of air-sea fluxes from a discus buoy, *J. Atmos. Oceanic Technol.*, *11*, 1144–1150.

Chapman, R., and F. M. Monaldo (1995), A novel wave height sensor, *J. Atmos. Oceanic Technol.*, *12*, 190–196.

Charnock, H. (1955), Wind stress on a water surface, *Q. J. R. Meteorol. Soc.*, *81*, 639–640.

Csanady, G. T. (2001), *Air-Sea Interaction*, 239 pp., Cambridge Univ. Press, New York.

Dobson, F. W., S. D. Smith, and R. J. Anderson (1994), Measuring the relationship between wind stress and sea state in the open ocean in the presence of swell, *Atmos. Ocean*, *32*, 237–256.

Donelan, M. A. (1990), Air-sea interaction, in *The Sea*, vol. 9, *Ocean Engineering Science*, edited by B. LeMéhauté and D. Hanes, pp. 239–292, John Wiley, Hoboken, N. J.

Donelan, M. A., and F. W. Dobson (2001), The influence of swell on the drag, in *Wind Stress over the Ocean*, edited by I. S. F. Jones and Y. Toba, pp. 181–189, Cambridge Univ. Press, New York.

Donelan, M. A., F. W. Dobson, S. D. Smith, and R. J. Anderson (1993), On the dependence of sea surface roughness on wave development, *J. Phys. Oceanogr.*, *23*, 2143–2149.

Donelan, M. A., W. M. Drennan, and K. B. Katsaros (1997), The air-sea momentum flux in conditions of wind sea and swell, *J. Phys. Oceanogr.*, *27*, 2087–2099.

Drennan, W. M., H. C. Graber, and M. A. Donelan (1999a), Evidence for the effects of swell and unsteady winds on marine wind stress, *J. Phys. Oceanogr.*, *29*, 1853–1864.

Drennan, W. M., K. K. Kahma, and M. A. Donelan (1999b), On momentum flux and velocity spectra over waves, *Boundary Layer Meteorol.*, *92*, 498–515.

Drennan, W. M., H. C. Graber, D. Hauser, and C. Quentin (2003), On the wave age dependence of wind stress over pure wind seas, *J. Geophys. Res.*, *108*(C3), 8062, doi:10.1029/2000JC000715.

Edson, J. B., C. W. Fairall, P. G. Mestayer, and S. E. Larsen (1991), A study of the inertial-dissipation method for computing air-sea fluxes, *J. Geophys. Res.*, *96*, 10,689–10,711.

Edson, J. B., A. A. Hinton, and K. E. Prada (1998), Direct covariance flux estimates from mobile platforms at sea, *J. Atmos. Oceanic Technol.*, *15*, 547–562.

Fairall, C. W., and S. E. Larsen (1986), Inertial-dissipation methods and turbulent fluxes at the air-ocean interface, *Boundary Layer Meteorol.*, *34*, 287–301.

Fairall, C. W., J. B. Edson, S. E. Larsen, and P. G. Mestayer (1990), Inertial-dissipation air-sea flux measurements: A prototype system using realtime spectral computations, *J. Atmos. Oceanic Technol.*, *7*, 425–453.

Fristchen, L. J., and L. W. Gay (1979), *Environmental Instrumentation*, pp. 2–9, Springer-Verlag, New York.

Fujitani, T. (1981), Direct measurement of turbulent fluxes over the sea during AMTEX, *Pap. Meteorol. Geophys.*, *32*, 119–134.

Garratt, J. R. (1977), Review of drag coefficient over oceans and continents, *Mon. Weather Rev.*, *105*, 915–929.

Hidy, G. M. (1972), A review of recent air-sea interaction research, *Bull. Am. Meteorol. Soc.*, *53*, 1083–1102.

Hwang, P. A. (2004), Influence of wavelength on the parameterization of drag coefficient and surface roughness, *J. Oceanogr.*, *60*, 835–841.

Hwang, P. A., and D. W. Wang (2004), Field measurements of duration limited growth of wind-generated ocean surface waves at young stage of development, *J. Phys. Oceanogr.*, *34*, 2316–2326.

Hwang, P. A., S. Atakturk, M. A. Sletten, and D. B. Trizna (1996), A study of the wavenumber spectra of short water waves in the ocean, *J. Phys. Oceanogr.*, *26*, 1266–1285.

Janssen, P. A. E. M. (1989), Wave-induced stress and the drag of air flow over sea waves, *J. Phys. Oceanogr.*, *19*, 745–754.

Large, W. G., and S. Pond (1981), Open ocean momentum flux measurements in moderate to strong winds, *J. Phys. Oceanogr.*, *11*, 324–336.

Large, W. G., and S. Pond (1982), Sensible and latent heat flux measurements over the ocean, *J. Phys. Oceanogr.*, *12*, 464–482.

Paulson, C. A., E. Leavitt, and R. G. Fleagle (1972), Air-sea transfer of momentum, heat and water determined from profile measurements during BOMEX, *J. Phys. Oceanogr.*, *2*, 487–497.

Smith, S. D. (1980), Wind stress and heat flux over the ocean in gale force winds, *J. Phys. Oceanogr.*, *10*, 709–729.

Smith, S. D. (1988), Coefficients for sea surface wind stress, heat flux, and wind profiles as a function of wind speed and temperature, *J. Geophys. Res.*, *93*, 15,467–15,472.

Smith, S. D., et al. (1992), Sea surface wind stress and drag coefficients: The HEXOS results, *Boundary Layer Meteorol.*, *60*, 109–142.

Stewart, R. W. (1974), The air-sea momentum exchange, *Boundary Layer Meteorol.*, *6*, 151–167.

Taylor, P. K., and M. Yelland (2001), The dependence of sea surface roughness on the height and steepness of the waves, *J. Phys. Oceanogr.*, *31*, 572–590.

Wang, D. W., and P. A. Hwang (2004), On the dispersion relation of short gravity waves from space-time wave measurements, *J. Atmos. Oceanic Technol.*, *21*, 1936–1946.

Williams, R. M., and C. A. Paulson (1977), Microscale temperature and velocity spectra in the atmospheric boundary layer, *J. Fluid Mech.*, *83*, 547–567.

Wu, J. (1980), Wind stress coefficients over the sea surface near neutral conditions: A revisit, *J. Phys. Oceanogr.*, *10*, 727–740.

Wyngaard, J. C. (1981), The effects of probe-induced flow distortion on atmosphere turbulence measurements, *J. Appl. Meteorol.*, *20*, 784–794.

Wyngaard, J. C., and O. R. Cote (1971), The budget of turbulence kinematic energy and temperature variances in the atmospheric surface layer, *J. Atmos. Sci.*, *28*, 190–201.

Yelland, M. J., and P. K. Taylor (1994), The use of the inertial dissipation technique for shipboard wind stress determination, *J. Atmos. Oceanic Technol.*, *11*, 1093–1108.

Yelland, M., and P. K. Taylor (1996), Wind stress measurements over the open ocean, *J. Phys. Oceanogr.*, *26*, 541–558.

————————————

P. A. Hwang and D. W. Wang, Oceanography Division, Naval Research Laboratory, Stennis Space Center, MS 39529, USA. (phwang@nrlssc.navy.mil; dwang@nrlssc.navy.mil)

J. Pan, Department of Environmental and Biomolecular Systems, Oregon Graduate Institute, 20000 NW Walker Road, Beaverton, OR 97006, USA. (panj@ebs.ogi.edu)